Southampton, UK, July 30 to August 2, 2019

STRUCTURE OF TURBULENT FLOWS ON HETEROGENEOUS IRREGULAR ROUGH SURFACES

Junlin Yuan
Department of Mechanical Engineering
Michigan State University
East Lansing, Michigan, USA
junlin@egr.msu.edu

Giles J. Brereton
Department of Mechanical Engineering
Michigan State University
East Lansing, Michigan, USA
brereton@egr.msu.edu

ABSTRACT

Direct numerical simulation data of turbulent half-channel flows over irregular roughness textures, either composed of a wide spectrum of wavelengths or small-wavelength-dominated, are used to identify the dependence of turbulence structure on the roughness texture. The present rough walls shorten the large, energy-containing scales in the outer layer, but do not modify the spectral characteristics of turbulence. Near the wall, roughness leads to weaker, smaller and more sparsely distributed low-speed streaks, as well as vortical structures that are preferentially located near the crest of high-slope, drag-generating roughness features. Results suggest that the basic growth mechanisms of new turbulence on a multiscale rough surface are fundamentally those on high-slope, small-scale roughness protuberances, only distributed differently by larger wavelengths.

INTRODUCTION

Most rough-wall studies on the mean-flow and turbulence structure are focused on regular, distributed roughness, which can be characterized by a single or a narrow set of dominant wavelengths. Relevant previous findings are summarized here. For an idealized obstacle, a mean recirculation region exists downstream of the obstacle, wrapped by a 3D shear layer where turbulence grows due to Kelvin-Helmholtz instability. For a distributed pyramid roughness, Talapatra & Katz (2012) showed experimental evidence of interacting U-shaped vortices of the scale of the pyramid. On a gravel bed, Mignot *et al.* (2009) observed mixing-layer dynamics in the wake of protuberances. The vorticity tensor becomes more isotropic near the wall, but not affected in the outer layer, indicating that the structure of small-scale turbulence is about the same as those on a smooth wall (Bhaganagar *et al.*, 2004). In addition, surface-induced mean secondary flows (or streamwise rollers) are first observed for turbine-blade roughness with large-scale spanwise heterogeneities of roughness height. Later systematic studies (e.g., Vanderwel & Ganapathisubramani (2015); Yang & Anderson (2018)) on organized distributed roughness with clear spanwise length scale, l_z, showed that the size of the secondary flow is of the scale of the boundary layer thickness (δ), if $l_z/\delta > 2$; for cases with $l_z/\delta < 0.2$, the turbulent statistics are similar to those on a homogeneous roughness.

Many naturally occurring rough surfaces are fractal-like (Passalacqua *et al.*, 2006). Recent development on how multiscale roughness textures affect turbulence is focused on the frictional drag and turbulence statistics inside the roughness sublayer. It is known that the drag mostly scales on wall-normal turbulence fluctuations at crest level (Orlandi *et al.*, 2006; Forooghi *et al.*, 2018), and large wavelengths do not produce drag (Barros *et al.*, 2018). For turbine-blade roughness (Yuan & Piomelli, 2014), filtered graphite surfaces (Busse *et al.*, 2015) and dissimilar random roughness (Forooghi *et al.*, 2018), it was shown that the anisotropies of Reynolds stress and dispersive stress tensors are texture-dependent. Also, Townsend's similarity is generally observed to apply to these statistics; but the extent of roughness sublayer varies.

In this work, we provide a detailed report on the structure of turbulence as affected by irregular roughnesses, either small-scale-dominated or multiscale. We examine characteristics of the mean secondary motions arising due to the surface heterogeneity, structure far from the wall, and the near-wall coherent motions including velocity streaks and vortices.

PROBLEM FORMULATION

The two rough surfaces considered are shown in Fig. 1(a) and 1(b): one is a synthesized sand-grain roughness model of Scotti (2006) and the other is assembled using a surface replicated from a hydraulic turbine blade. The latter displays a surface-height power spectrum decay rate of around -2 with the largest wavelength much larger than δ; therefore, the turbine-blade roughness resembles a wide-spectrum, fractal geometry (Passalacqua *et al.*, 2006) and is called a 'multiscale roughness' herein. In comparison, the sand-grain geometry is dominated by scale of $o(0.1\delta)$.

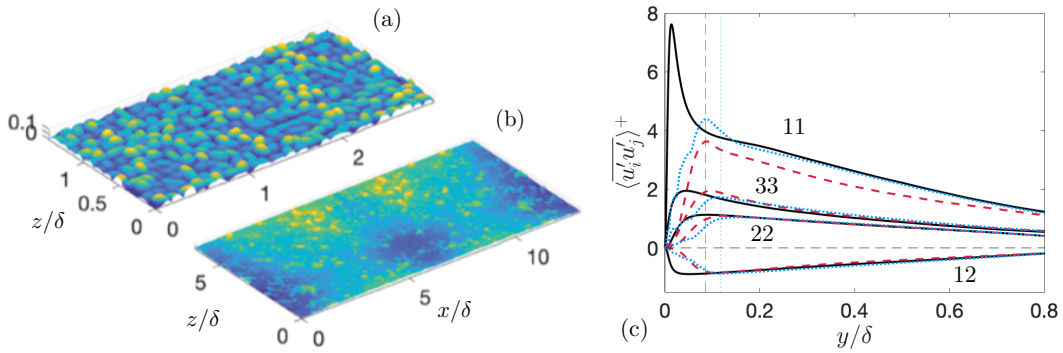

Figure 1. Rough surfaces colored by height of (a) 1/4 of sand-grain surface, (b) 1/2 of turbine-blade (multiscale) surface. (c) Reynolds stress tensor components; vertical lines indicate crest height. ——— Smooth, - - - sand grains, - - - multiscale roughness.

Table 1. Case summary. Superscript "+" indicates normalization in wall units. L_x, L_z are domain sizes.

Surface	k_s^+	$(L_x, L_z)/\delta$	$(\Delta x^+, \Delta y^+_{\min}, \Delta z^+)$
Smooth	–	$(6,3)$	$(11.7, 0.3, 5.8)$
Sand-grain	78	$(6,3)$	$(6.0, 0.7, 6.0)$
Multiscale	24	$(13,13)$	$(13.0, 0.8, 13.0)$

The two surfaces are scaled to achieve the same mean (Ra) and root-mean-square heights (k_{rms}), similar crest heights (of around 0.1δ), and are both peaky. However, the multiscale surface is characterized by significantly lower effective slopes in both streamwise (x) and spanwise (z) directions, due to the involvement of large wavelengths. It can be shown that the multiscale surface produces significantly lower frictional drag than the sand grains (Yuan & Aghaei Jouybari, 2018).

The parameters of all cases are summarized in Table 1. The frictional Reynolds number $Re_\tau = 1000$ for all cases. The roughness Reynolds number, k_s^+, is sufficient to reach the fully rough regime for both rough cases. A larger domain size is used for the multiscale surface to accommodate the large wavelengths. We solve the equations of conservation of mass and momentum governing the incompressible flow of a Newtonian fluid. A discrete-forcing immersed-boundary method is used to impose the no-slip rough-wall boundaries on a Cartesian grid. The double-averaging (DA) decomposition (Raupach & Shaw, 1982) is employed to separate the form-induced fluctuations from the turbulent ones, $\theta(x,y,z,t) = \langle\overline{\theta}\rangle(y) + \widetilde{\theta}(x,y,z) + \theta'(x,y,z,t)$, where $\langle\overline{\theta}\rangle$ is the (intrinsic) plane-and-time average of a variable θ, $\widetilde{\theta}$ is the form-induced perturbation of the time average, and θ' is the stochastic, turbulent fluctuation. The total number of grid points amounts to 70 to 120 million. Statistics are collected during relatively long simulation time of $40-80\delta/u_\tau$, where u_τ is the friction velocity.

RESULTS

Outer-layer structure

The roughness sublayer (RSL) is defined herein as the region in which the form-induced perturbations are significant ($\widetilde{u}$ rms higher than $0.06\langle\overline{u}\rangle$). The region above this threshold is considered as the outer layer, which starts at around $y/\delta = 0.12$. In this section, we show that the imposed surface roughnesses herein do not fundamentally change the structure of turbulence in the outer layer, despite noticeable discrepancies in the Reynolds stresses (Fig. 1b) and two-point velocity correlation from the smooth case.

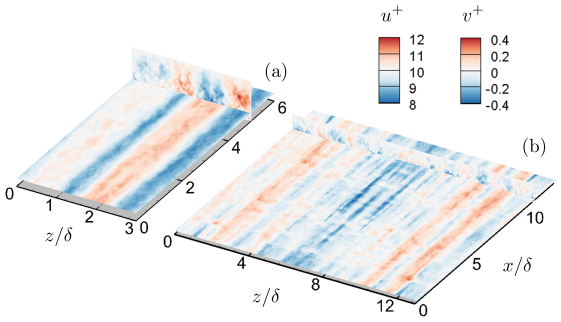

Figure 2. Horizontal contours of $\overline{u}^+$ at $y/\delta = 0.2$ and vertical contours of $\overline{v}^+$ for (a) sand-grain and (b) multiscale roughnesses.

The large secondary motions of time-averaged flow develop on both surfaces (Fig. 2), even for the sand-grain roughness which does not show any dominant spanwise length scale of order of δ. These motions are characterized by positive and negative $\overline{v}$ regions extending for the majority of the boundary layer, corresponding to low (low-momentum pathways) and high $\overline{u}$ values (high-momentum pathways), respectively. Such motions appear to be affected by the large z wavelengths of the surface only, insensitive to the large x wavelengths. Their irregular positioning along z arises from the randomness of the surface; the spanwise separation between alternating low and high momentum regions are at least 1δ.

The extent of the large-scale motions of turbulence are compared using two-point u' autocorrelations in Fig. 3, showing significant decreases of the streamwise length scale at $(y-d)/\delta = 0.3$ on account of both roughness geometries. This is not unreasonable as the large secondary motions effectively extend the region of roughness effects father from the wall. In addition, the roughness heights exceed the usually accepted values for validity of Townsend's similarity ($k/\delta < 20$).

The energy distribution among different scales outside the RSL is shown using the premultiplied power spectra.

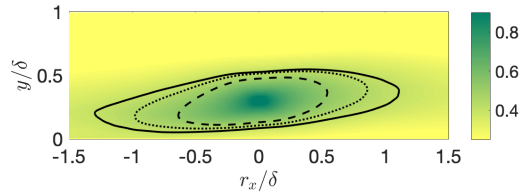

Figure 3. Two-point autocorrelations of u' at $(y-d)/\delta = 0.4$ for smooth (contour and ———), sand-grain (- - -) and multiscale roughness (-·-) cases. d is the virtual origin. Contour lines show level 0.4.

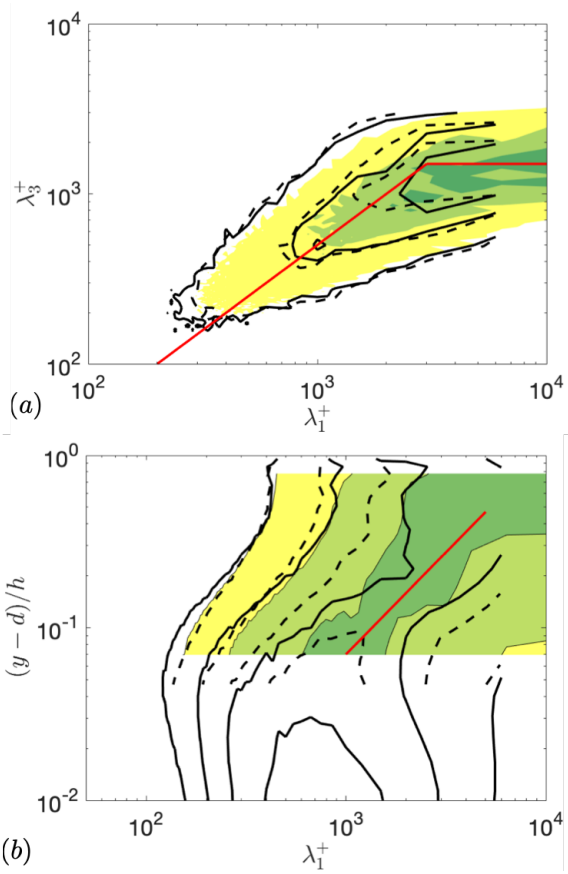

Figure 4. (a) 2D premultiplied power spectra of u' at $(y-d)/\delta = 0.4$ for smooth (———), sand-grain (- - -) and multiscale (contour) cases. Red lines: $\lambda_x = 2\lambda_z$ and $\lambda_z = 1.50\delta$. (b) Normalized premultiplied power spectrum variation in y. Red line: $\lambda_x \sim (y-d)/\delta$. Contour levels: 0.25(0.25)0.75 times of maximum value.

2D power spectra of u', $\kappa_x\kappa_z\langle|\widehat{u}\widehat{u}^*|\rangle$, at $y = 0.4\delta$ (Fig. 4a) display the same characteristics between all cases. Here, κ_i and λ_i are the wavenumber and wavelength in x_i direction. Two types of mode of u' motions are present in the outer layer (del Álamo & Jiménez, 2003): long anisotropic structures with its spanwise wavelength (λ_z) of 1.50δ (as compared to 1.75δ observed by del Álamo & Jiménez (2003)) and quasi-isotropic modes with $\lambda_x \approx 2\lambda_z$. Modes with $\lambda_x \approx \lambda_z$ are also observed for v' and w' power spectra (not shown). Roughness does not lead to fundamental change of the spectral densities above roughness crest, albeit the size of large-scale turbulent motions are decreased.

We also show here that roughness does not qualitatively modify the linear growth of the characteristic streamwise wavelength along y. Figure 4(b) shows the 1D normalized power spectrum of u', $\kappa_1\langle\widehat{u}\widehat{u}^*\rangle/\langle\overline{u'^2}\rangle$, obtained by integrating the 2D spectrum along κ_3. Quantitative differences among the three cases can be seen in the outer layer corresponding to very large scale motions of size $o(\delta)$ only. The length scale defined by locations of the spectral maxima at each y grows linearly in the region $y/\delta < 0.3$. This is consistent with observations of Jiménez & Hoyas (2008) and gives further evidence that rough surfaces of the two textures do not change the main spectral characteristics of turbulence far from the wall.

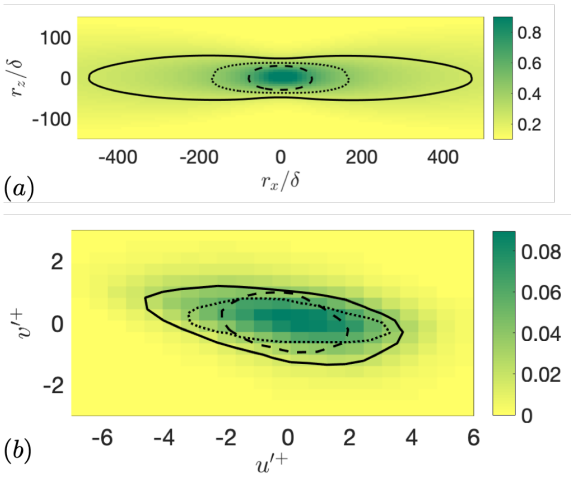

Figure 5. (a) Two-point autocorrelations of u' at $y^+ = 30$. Contour lines show level 0.25. (b) Joint probability distribution functions of u' and v' at $y^+ = 30$. Contour lines show level 0.025. See Fig. 3 for legends.

Low-speed streaks

It is often observed that in the RSL the Reynolds stress tensor is of the shape of an oblate spheroid due to more significantly damped u' than the other two components (for example, see Busse & Sandham (2012)) and that the streaks are shortened. However, it is not clear whether the damped u' rms is due to milder u' intensity or higher intermittency of the low-speed streaks.

Figure 5a compares the two-point autocorrelations of u', $R_{uu}(r_x, r_z)$, at $y^+ = 30$; this location is of interest since the roughness effect on damping u' rms is significant. Care is taken so that the quantity values inside the solid regions do not contribute to the statistics shown herein. Results indicate that streaks are dramatically shortened in x (more so for the sand-grain roughness) and slightly narrowed in z. In addition, the fluid area fraction occupied by low-speed fluid (identified here as region with $u^+ < -1$) at this elevation decreases noticeably from 37% on a smooth wall to 11% on sand grains and 25% on the multiscale roughness, suggesting that the streaks are not only shorter, but also farther apart.

The intensity of u' inside the low-speed streaks is compared using the joint probability distribution functions of u' and v' at the same elevation (Fig. 5(b)). The intermittent events with intense, negative u' and weaker, positive v' are associated with the low-speed streaks. For both rough cases the u'^+ intensity inside low-speed streaks is lower than the smooth case, more so for the sand-grain case. To-

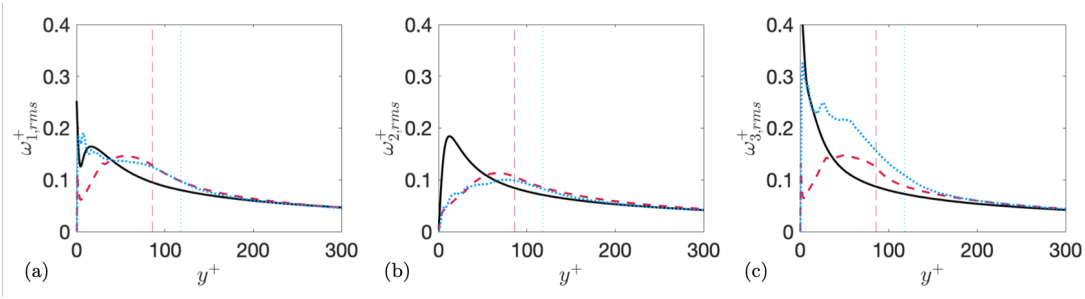

Figure 6. Root-mean-square vorticity fluctuations. —— Smooth, - - - sand grains, - - - multiscale roughness.

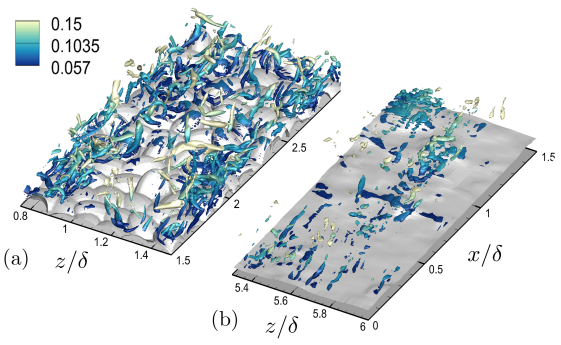

Figure 7. Vortical structures visualized as isosurfaces of negative λ_2 colored by y/δ for (a) sand-grain and (b) multiscale-roughness cases.

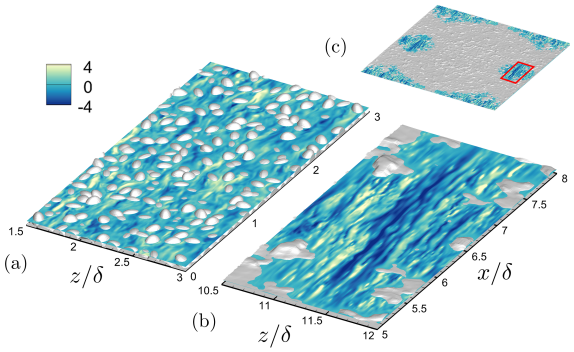

Figure 8. Contours of u'^+ at $y/\delta = 0.04$ (slightly below d) for (a) sand-grain and (b) multiscale-roughness cases; the latter is zoomed out in (c) to show full domain.

gether, these observations indicate weaker and smaller velocity streaks of sparser distribution inside the RSL compared to the same elevation on a smooth wall.

Vorticity and vortical structures

Vorticity fluctuations, ω_i, account for the turbulent structure. Near the wall, ω_3 is mostly caused by the intense shear generated by u' between the wall and the streaks, ω_2 represents mostly $\partial_z u'$ in the regions between adjacent high and low-speed streaks, and ω_x displays a local minimum and a local maximum at $y^+ = 5$ and 20, attributed to the quasi-streamwise vortices on a smooth wall.

Trends to isotropic vorticity fluctuations due to roughness have been observed. The same trend is displayed by the sand-grain case in Fig. 6. The peak of ω_1 rms is displaced towards the crest location from the smooth wall profile; this can be explained by the displaced elevation of intense vortex stretching by the shear of the DA velocity. As a result, in the lower portion of the RSL, these vortices are sparse, leading to very weak rms of ω_1. In addition, the weaker rms values of ω_2 and ω_3 near the wall are due to the velocity streaks being less intense, smaller in size and sparser in distribution as shown above.

In contract, the vorticity fluctuations in the RSL of the multiscale roughness maintain higher anisotropy near the wall. Here, low-speed streaks with intense u' are still present below $y = d$ in the recessed roughness region (due to the largest x wavelengths of roughness), as shown in Fig. 8(b). Due to the lack of large wavelengths, these structures are mostly not permissible in the lower portion of the RSL of the sand-grain flow. The streaks in these regions are weaker than the smooth case at the same elevation, producing lower $\partial_z u'$ and $\partial_y u'$ and, consequently, weaker ω_2 and ω_3 at the wall.

We note another difference between the rough and smooth cases. Near the crest in both rough cases, the flows in RSL are affected by local proximity of the roughness surface located below; these regions are associated with stronger $\partial_y u'$, leading to higher ω_3 rms in the rough-wall cases near the crest.

Visualizations of the vortical structures are shown in Fig. 7. On rough surfaces, these structures display larger variance in their orientation than in the smooth case (not shown), consistent with the picture of interacting U-shape vortices (Talapatra & Katz, 2012). In addition, these structures are mostly distributed near or above the crest, rarely occurring below d. A significant difference between the two rough cases is that, compared to the densely distributed vortical structures around sand grains, on the multiscale roughness they are clustered in the wake of steep, small-wavelength peaks, and mostly absent in other areas. This is also demonstrated by the intermittency of vortical structures in Fig. 10.

To provide insight into why the vortices are rare below $y = d$, the production terms of $\langle\overline{\omega_1^2}\rangle$ are shown in Fig. 9. The total production is

$$\mathscr{P}_{11} = -2\overline{u_j'\omega_1}\Omega_{j,1} + 2\overline{\omega_1\omega_j u'_{,j}} + 2\overline{\omega_1\omega_j}\,\overline{u}_{,j} + 2\overline{\omega_1 u'_{,j}}\Omega_j, \quad (1)$$

where Ω_i is the mean vorticity and the four terms on the right-hand-side are, respectively, the gradient production ($\mathscr{P}_g$), turbulence stretching ($\mathscr{P}_s^t$), time-mean-flow stretching ($\mathscr{P}_s^{\overline{u}}$), and the mixed production ($\mathscr{P}_m$). In the RSL, the plane average of $\mathscr{P}_s^{\overline{u}}$ can be decomposed to two terms representing the stretching due to the DA velocity ($\mathscr{P}_s^{da}$) and that due to the form-induced (wake) velocity ($\mathscr{P}_s^{w}$), respec-

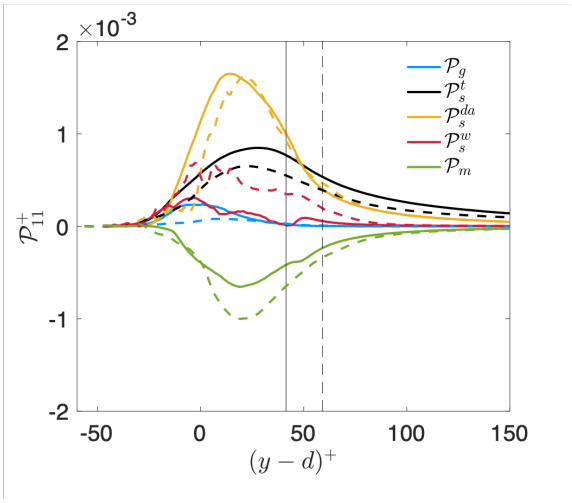

Figure 9. Superficially averaged production terms of $\langle\overline{\omega_1^2}\rangle$ budget for sand grains (———) and multiscale roughness (– – –).

tively,

$$\langle\mathscr{P}_s^{\overline{u}}\rangle = 2\langle\overline{\omega_1\omega_j}\rangle\langle\overline{u}\rangle_{,j} + 2\langle\widetilde{\omega_1\omega}_j\widetilde{u}_{,j}\rangle. \qquad (2)$$

Interestingly, the most important production comes from stretching due to the DA shear. Within the RSL, it is often observed that the streamwise DA velocity displays either a linear-like or exponential profile with an inflection point located inside the RSL or near the crest (Nikora *et al.*, 2004)—the former is the case with the present roughnesses. The high mean shear associated with the inflection point leads to intense ω_1 magnitudes by vortex stretching; this takes place near the crest elevation. In comparison, stretching due to wake velocity is non-zero, but small for the sand-grain case. It is, however, significant for the case with the multiscale roughness. At a given elevation, the high speed region corresponding to the trough of large wavelength is associated with $\overline{u}$ higher than the DA value at this y (i.e., positive $\widetilde{u}$). As a result, the wall-normal shear of the time-mean velocity contributes to P_s^w through $\partial_y\widetilde{u}$. In the lower portion of the RSL of the multiscale-roughness flow, P_s^w is the dominant source term.

Positioning of coherent motions

The intermittencies of near-wall streaks and vortical structures are calculated as the fractions of time during which these events occur at each (x,z) location for $y/\delta \in [0,0.2]$. The streaks are identified as $u'^+ < -0.1$; the vortical structures are identified as regions with $\lambda_2\delta^2/u_\tau^2 < 1E-4$ and $|\omega_x|/|\boldsymbol{\omega}| \geq 0.8$. The vortical structures predominantly oriented along z are also evaluated, giving the same observations as follows.

Over a roughness with spanwise heterogeneity, the high momentum pathways were often observed to coincide with regions of enhanced Reynolds stresses and elevated roughness. The secondary motions are both driven and sustained by the spanwise variation in imposed aerodynamic drag from the topography, leading to the spatial gradients in the Reynolds-stress components (Anderson *et al.*, 2015).

On the multiscale roughness, comparing the (x,z) drag distribution (not shown) and $\overline{u}$ contours (Fig. 2(b)) shows

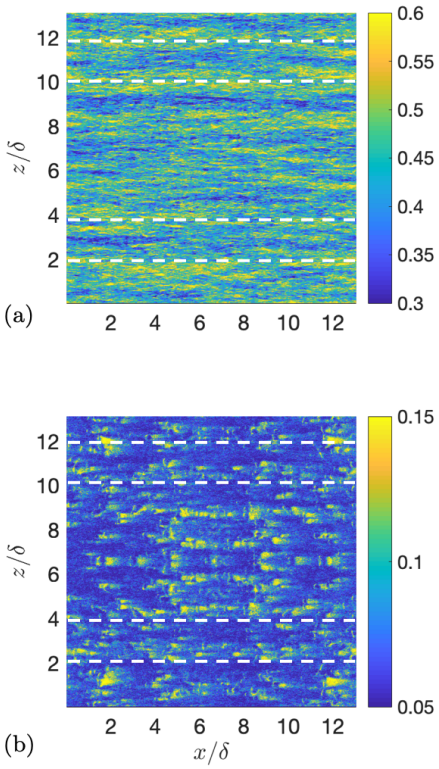

Figure 10. Intermittencies of (a) low-speed streaks and (b) vortical structures with $\boldsymbol{\omega}$ predominantly oriented in x for the multiscale case. Dashed line highlights high-momentum pathways.

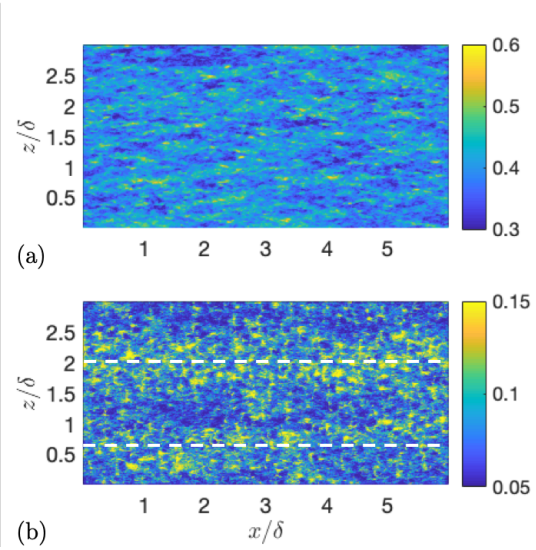

Figure 11. Some plots as Fig. 11 for sand-grain roughness.

the same picture depicted above. Here, we also show that regions of high drag coincide with high intermittency of near-wall vortical structures (consistent with the enhanced Reynolds stresses) and the preferred spanwise locations of low-speed streaks. Such dependence on roughness features indicates two possibilities of turbulence generation:

(1) the roughness-induced mean shear and channeling generate mixing-layer vortices and U-shape vortices (Talapatra & Katz, 2012), which, in turn, through their spatial alignment induce low-speed streaks, or (2) the autonomous cycle of low-speed streaks and quasi-streamwise vortices on a smooth wall (Jiménez & Pinelli, 1999) is, to some extent, still present but is initiated by roughness peaks. Either way, the evidences point toward a key role played by high-slope, small-scale topological features in generating and sustaining turbulence.

Around sand grains, the same phenomenon appears to be present. The intermittency of vortices appears to pick up the heterogeneity of drag ditribution in (x,z), though much more subtle, and leads to pathways of high and low values of mean momentum. The streak distribution, however, is more smeared (showing no discernible preferred location), probably related to the fact that the vortical structures are more homogeneously distributed than for the multiscale roughness.

CONCLUSIONS

Existing work on effects of multiscale roughness (with wavelengths larger than δ) on turbulence is mostly focused on the statistical description and structural change of the outer layer. In this work, we characterize the structural dependence on irregular roughness textures, multiscale or otherwise, throughout the boundary layer.

Results show that, despite a decrease of size of δ-scale coherent motions in the outer layer on a rough wall, the present rough surfaces do not fundamentally alter the spectral characteristics of turbulence. Near the wall, large streamwise roughness wavelengths allow intense low-speed streaks to penetrate deep into the roughness sublayer; this leads to anisotropic vorticity fluctuations near the wall. In additional, a high intermittency of vortical structures is found in regions of small-wavelength, peaky roughness features that also produce drag. The effect of large surface scales comes in by introducing spanwise intervals larger than δ to the distribution of these regions, which in turn lead to large-scale mean secondary flows due to associated Reynolds stress gradients. Low-speed streaks occur preferentially in such regions also, suggesting that the small surface wavelengths play a key role in near-wall turbulence generation. These observations suggest that the basic growth mechanisms of new turbulence on a multiscale rough surface are fundamentally those on small-scale roughness protuberances, only distributed differently by larger wavelengths.

ACKNOWLEDGMENTS

The authors acknowledge the Office of Naval Research, program manager Thomas Fu, for the financial support. Mostafa Aghaei Jouybari is thanked for DNS data processing.

REFERENCES

del Álamo, J. C. & Jiménez, J. 2003 Spectra of the very large anisotropic scales in turbulent channels. *Phys. Fluids* **15** (6), L41–L44.

Anderson, W., Barros, J. M., Christensen, K. T. & Awasthi, A. 2015 Numerical and experimental study of mechanisms responsible for turbulent secondary flows in boundary layer flows over spanwise heterogeneous roughness. *J. Fluid Mech.* **768**, 316–347.

Barros, J. M., Schultz, M. P. & Flack, K. A. 2018 Measurements of skin-friction of systematically generated surface roughness. *Int. J. Heat Fluid Flow* **72**, 1–7.

Bhaganagar, K., Kim, J. & Coleman, G. N. 2004 Effect of roughness on wall-bounded turbulence. *Flow, Turbul. Combust.* **72**, 463–492.

Busse, A., Lützner, M. & Sandham, N. D. 2015 Direct numerical simulation of turbulent flow over a rough surface based on a surface scan. *Comput. Fluids* **116**, 129–147.

Busse, A. & Sandham, N. D. 2012 Parametric forcing approach to rough-wall turbulent channel flow. *Journal of Fluid Mechanics* **712**, 169–202.

Forooghi, P., Stroh, A., Schlatter, P. & Frohnapfel, B. 2018 Direct numerical simulation of flow over dissimilar, randomly distributed roughness elements: A systematic study on the effect of surface morphology on turbulence. *Phys. Rev. Fluids* **3**, 044605–1–27.

Jiménez, J. & Hoyas, S. 2008 Turbulent fluctuations above the buffer layer of wall-bounded flows. *J. Fluid Mech.* **611**, 215–236.

Jiménez, J. & Pinelli, A. 1999 The autonomous cycle of near-wall turbulence. *J. Fluid Mech.* **389**, 335–359.

Mignot, E., Hurther, D. & Bartheleemy, E. 2009 On the structure of shear stress and turbulent kinetic energy flux across the roughness layer of a gravel-bed channel flow. *J. Fluid Mech.* **638**, 423–452.

Nikora, V., Koll, K., McEwan, I., McLean, S. & Dittrich, A. 2004 Velocity distribution in the roughness layer of rough-bed flows. *J. Hydr. Engng* **130**, 1036–1042.

Orlandi, P., Leonardi, S. & Antonia, R. A. 2006 Turbulent channel flow with either transverse or longitudinal roughness elements on one wall. *J. Fluid Mech.* **561**, 279–305.

Passalacqua, P., Porté-Agel, F., Foufoula-Georgiou, E. & Paola, C. 2006 Application of dynamic subgrid-scale concepts from large-eddy simulation to modeling landscape evolution. *Water Resour. Res.* **42**, W06D11–1–11.

Raupach, M. R. & Shaw, R. H. 1982 Averaging procedures for flow within vegetation canopies. *Bound.-Lay. Meteorol.* **22**, 79–90.

Scotti, A. 2006 Direct numerical simulation of turbulent channel flows with boundary roughened with virtual sandpaper. *Phys. Fluids* **18**, 031701–1—4.

Talapatra, S. & Katz, J. 2012 Coherent structures in the inner part of a rough-wall channel flow resolved using holographic PIV. *J. Fluid Mech.* **711**, 161–170.

Vanderwel, C. & Ganapathisubramani, B. 2015 Effects of spanwise spacing on large-scale secondary flows in rough-wall turbulent boundary layers. *J. Fluid Mech.* **774**, R2.

Yang, J. & Anderson, W. 2018 Numerical study of turbulent channel flow over surfaces with variable spanwise heterogeneities: Topographically-driven secondary flows affect outer-layer similarity of turbulent length scales. *Flow, Turb. Combust.* **100**, 1–17.

Yuan, J. & Aghaei Jouybari, M. 2018 Topographical effects of roughness on turbulence statistics in roughness sublayer. *Phys. Rev. Fluids* **3**, 114603.

Yuan, J. & Piomelli, U. 2014 Estimation and prediction of the roughness function on realistic surfaces. *J. Turbul.* **15**, 350–365.